Keratin network modifications lead to the mechanical stiffening of the hair follicle fiber

Thomas Bornschlögl[a], Lucien Bildstein[a,1], Sébastien Thibaut[a], Roberto Santoprete[a], Françoise Fiat[a], Gustavo S. Luengo[a], Jean Doucet[b], Bruno A. Bernard[a], and Nawel Baghdadli[a]

[a]L'Oreal Research & Innovation, F93600 Aulnay-sous-Bois, France; and [b]Laboratoire de Physique des Solides, Paris-Sud University, F91400 Orsay, France

Edited by David A. Weitz, Harvard University, Cambridge, MA, and approved March 15, 2016 (received for review October 29, 2015)

The complex mechanical properties of biomaterials such as hair, horn, skin, or bone are determined by the architecture of the underlying fibrous bionetworks. Although much is known about the influence of the cytoskeleton on the mechanics of isolated cells, this has been less studied in tridimensional tissues. We used the hair follicle as a model to link changes in the keratin network composition and architecture to the mechanical properties of the nascent hair. We show using atomic force microscopy that the soft keratinocyte matrix at the base of the follicle stiffens by a factor of ∼360, from 30 kPa to 11 MPa along the first millimeter of the follicle. The early mechanical stiffening is concomitant to an increase in diameter of the keratin macrofibrils, their continuous compaction, and increasingly parallel orientation. The related stiffening of the material follows a power law, typical of the mechanics of nonthermal bending-dominated fiber networks. In addition, we used X-ray diffraction to monitor changes in the (supra)molecular organization within the keratin fibers. At later keratinization stages, the inner mechanical properties of the macrofibrils dominate the stiffening due to the progressive setting up of the cystine network. Our findings corroborate existing models on the sequence of biological and structural events during hair keratinization.

atomic force microscopy | elastic modulus | human hair follicle | biomechanics | X-ray diffraction

Biological tissues are structurally complex materials with remarkable mechanics and elastic moduli that can range from a few pascals to several gigapascals (1–3). An active field aims at understanding how the local structural and mechanical properties of bionetworks define its macroscopic mechanics from a molecular scale toward a cellular and tissue scale (4–6). One challenge is that the properties of these networks have to be considered over multiple length and force scales with macroscopic mechanical forces being transduced from the whole tissue scale down to the cellular and molecular level and vice versa.

At the cellular level, the last decades witnessed for a considerable advancement toward a better understanding of how the cytoskeleton composed of actin, microtubules, and intermediate filaments (IFs) determines cellular mechanics (1, 6–8). In vitro studies on isolated cells (6) and reconstituted in vitro bionetworks with controllable architecture and composition (9–12) considerably advanced our knowledge of cytoskeletal mechanics. However, these models are only approximations of the complex tridimensional architecture of most tissues. At the tissue level, the mechanical anisotropy together with the variety of mechanically different constituents usually hamper direct correlations between network architecture and mechanical properties (3, 13). Analytical models and computer modeling allow to theoretically link the macroscopic mechanical properties of the network with parameters of the local network architecture (5, 14, 15).

The human hair follicle was used here as a model system to show how the local, microscopic network architecture is connected to local mechanical properties in a tridimensional tissue. The stiffness of the hair follicle is expected to extend over several orders of magnitude, due to the differentiation of its soft keratinocytes into a hair fiber with Young moduli in the gigapascal range (16, 17). Between these two extremes, the keratinization process of the IF network transforms a living isotropic cell matrix into an inert and anisotropic material (18), bridging length and force scales from the subcellular level to the tissue level. This transition shares similarities with the formation of other keratinized structures such as nails and horn and with the formation of the stratum corneum, the outermost layer of the skin. It is accompanied by multiple biological processes such as a specific expression of different keratins and keratin-associated proteins (KAPs) (19) that lead, together with the reorganization of the keratin network and the loss of water, to a compaction and hardening of the fiber. However, although several complementary studies analyzed the changes in the network architecture accompanying the keratinization process (20–22), little is known about the consequence, its mechanical hardening.

To address this, we used atomic force microscopy (AFM) to measure the hardening of the keratin structure along the follicle axis while simultaneously quantifying the local keratin network architecture, as well as the keratin supramolecular organization.

Results

Follicle Mechanics. In a first step, the stiffening of the keratin network was quantified throughout human hair follicles dissected from healthy white individuals. Longitudinal 10-μm-thick sections were obtained by cryotomy and adsorbed onto glass slides. To mimic in vivo conditions, the water content had to be kept high to prevent tissue drying and collapse. Thus, after cutting, we immediately immersed the sections in PBS solution (Fig. 1*A* and Fig. S1*A*). AFM examination of the immersed sections allows a local probing of mechanical properties due to a sharp tip with a radius in the

Significance

Mechanical properties of tissues often emerge from fibrous protein networks spanning multiple cell lengths. For the first time, to our knowledge, atomic force microscopy was used to measure the mechanical properties of the human hair follicle. We find a considerable stiffening along the first millimeter that we link to changes in the keratin network architecture and composition. In early keratinization stages, the thickening, densification, and increasing orientation of fibers are responsible for the mechanical stiffening, whereas in later stages, intermolecular cross-linking becomes predominant. Our results corroborate the known biological and structural events during hair keratinization and underline the link between the mechanical properties of the hair follicle and its multiscale tridimensional organization.

Author contributions: L.B. and N.B. designed research; T.B., L.B., S.T., F.F., and J.D. performed research; T.B. and L.B. contributed new reagents/analytic tools; T.B., L.B., R.S., and J.D. analyzed data; and T.B., L.B., R.S., G.S.L., and B.A.B. wrote the paper.

Conflict of interest statement: T.B., L.B., S.T., R.S., F.F., G.S.L., B.A.B., and N.B. are employees of L'Oreal.

This article is a PNAS Direct Submission.

Freely available online through the PNAS open access option.

[1]To whom correspondence should be addressed. Email: lbildstein@rd.loreal.com.

This article contains supporting information online at www.pnas.org/lookup/suppl/doi:10.1073/pnas.1520302113/-/DCSupplemental.

nanometer range (r = 20–60 nm). We used the force-volume mode in which force and indentation depth were recorded for 256 equidistant approach curves within regions of 10 × 10 μm^2 (Fig. S1 *A* and *B*). The related elastic moduli are calculated using the Hertz model (*SI Text*) (23, 24). Note that the determined absolute moduli values depend on the tip shape and the used fitting model; sharp tips are expected to rather probe the local mechanics of the underlying fibrous network (*SI Text*) (25–27). The deduced elastic moduli recorded along the follicle axis are shown as boxplots in Fig. 1*A*. The large dispersion of moduli within one 10 × 10-μm^2 region arises from inhomogeneities on the nanometer scale of the sample and prompts the averaging over the recorded force indentation curves to be a representative measurement for the local follicle mechanics (Fig. S1*H*).

Fig. 1*A* shows an increase of the elastic modulus by almost three orders of magnitude along the first millimeter of a representative hair follicle. This observation was validated on 25 sections, of 12 follicles obtained from three different donors, and is summarized in Fig. 1*B*. The mean stiffness of 30 ± 23 kPa obtained in the keratinocyte matrix of the bulb increases to 11 ± 10 MPa measured on the plateau (distances > 800 μm) of the differentiated hair immersed in PBS. In vivo, the hair would in addition dry at the latest when protruding from the scalp. The related stiffening leads to 2.7 ± 1.4 GPa (Fig. 1*B*), measured at distances above 800 μm after drying of the follicles (*SI Text*). Note that the modulus of the developing, dried hair measured from 800 μm on is similar to moduli determined on mature hair (16, 28).

To quantify the stiffness increase throughout the follicle and to compare different samples, we fitted a sigmoid Hill function to the logarithmic data of individual follicle cuts (*SI Text*; red line in Fig. 1*A*). The low variability of the position of the inflection point of the sigmoidal function (k = 512 ± 150 μm; Fig. 1*C*) shows that the mechanical hardening of the hair fiber reproducibly takes place in the first millimeter of the follicle and suggests that it follows the same general mechanism even for different donors. To quantify the functional form of the moduli increase in the keratinization zone, we plotted for all measured follicles the mean moduli at a specific distance relative to their individual inflection point k_i (black dots in Fig. 1*D*). On average, the moduli show a linear dependence with a slope of 4.4 ± 1.3 in a log-log plot, arguing for a power law behavior $E \sim x^{4.4}$ for the mechanical hardening of the fiber.

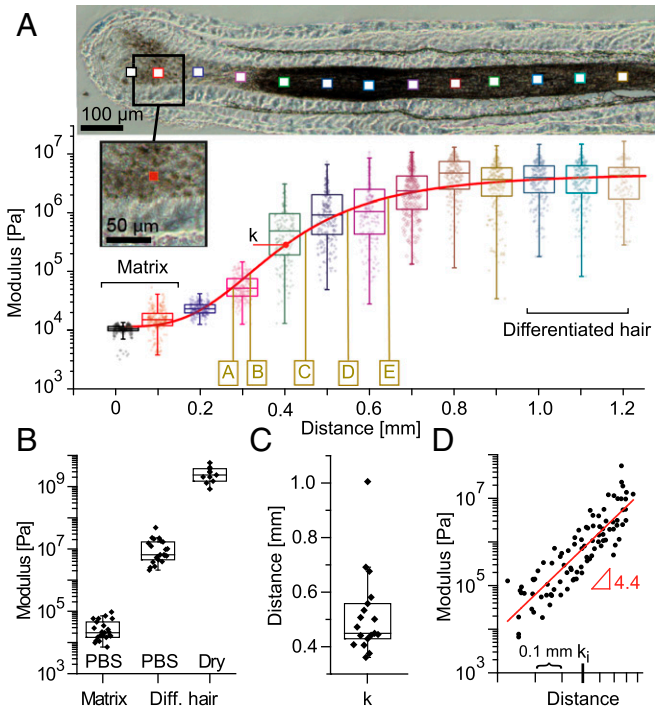

Fig. 1. Mechanical characterization of the hair follicle. (*A*) Elastic modulus map for increasing distances along one follicle. Boxplots depict the moduli obtained from 256 force-indentation curves measured in equidistant positions within the corresponding 10 × 10-μm^2 areas represented by squares on the optical microscopy picture (actual size depicted in the higher-magnification *Inset*). The red curve is a sigmoidal function fitted to the logarithmic data (*SI Text*); k denotes the position of the inflection point. The brown letters denote approximate positions where images shown in Fig. 2 were recorded on the same follicle. (*B*) Boxplots of the mean moduli measured on different follicles in the keratinocyte matrix and on the plateau (distances > 800 μm) in PBS (n = 25) or after drying the sections (n = 9). (*C*) Position of the inflection point for different follicles, (n = 18). (*D*) Moduli increase between ~200- and ~900-μm distances from different follicles shown in a log-log plot. Every point corresponds to the mean of a probed 10 × 10-μm^2 zone. The traces are aligned on the x axis to their respective inflection points k_i (n = 18).

Changes in Network Architecture During Keratinization. To understand how the observed macroscopic hardening of the hair follicle corresponds to microscopic changes in the keratin network architecture, topographic images of longitudinal sections of hair follicles were recorded along their axis. AFM enables high-resolution images to be recorded without the ultrathin sectioning or staining required for transmission electron microscopy (TEM) (Figs. S2 and S3), which already revealed profound changes in the IF network (29, 30). The topographic images were obtained using the peak force quantitative nanomechanical mapping (QNM) mode of the AFM on dried follicles that retain the fiber-network architecture (Fig. S4). Fig. 2 shows representative topographic images at increasing distances from the follicle bulb. The network appears above ~170 μm (Fig. 2*A*), with an architecture that changes along the keratinization process: fibers become thicker, more aligned, and more densely packed. A TEM study revealed consistent changes (Fig. S2).

To quantify these observations, the diameter of macrofibrils and their orientation were measured from height profiles of randomly chosen filaments in sections of seven different follicles (Fig. 3*A*). The mean macrofibril diameter increases from 137 ± 42 nm (distance 200 μm) to a plateau value of 333 ± 84 nm above 500 μm (Fig. 3*B*). Analysis of TEM data revealed a similar evolution (Fig. S3*A*). Imaging of a 10-μm-wide stripe along 760 μm of a single follicle section shows that the macrofibril diameter increases continuously below a distance of 500 μm (Figs. S5 and S6). The preferential orientation of the fibers was analyzed by calculating the decay length of the autocorrelation function along different angles. The ratio of the shortest to the longest autocorrelation decay for two specific angles (Fig. 3*C*) is related to the preferential orientation of fibers relative to the follicle axis. Consistently with Fig. 2, the keratin network below 500 μm shows some degree of anisotropy, whereas the fibers become predominantly aligned in parallel above 500 μm. In addition, a compaction of the network can be observed along the follicle axis (Fig. 2 and Fig. S3*B*), indicating an increasing volume fraction of macrofibrils. To quantify the volume fraction of keratin-containing macrofibrils, we used synchrotron FTIR microspectroscopy as a direct local measurement of keratin concentration along the follicle. Spectra were recorded in dried sections of six different follicles, and the baseline-corrected absorbance of the amide I band in the α-helical region (1,652 cm^{-1}) was plotted (a representative dataset is shown in Fig. 3*D*). A linear increase in the keratin filament volume concentration is observed along the follicle axis for the first 700 μm, after which a saturation of the FTIR signal is reached due to the linearly increasing thickness of the section.

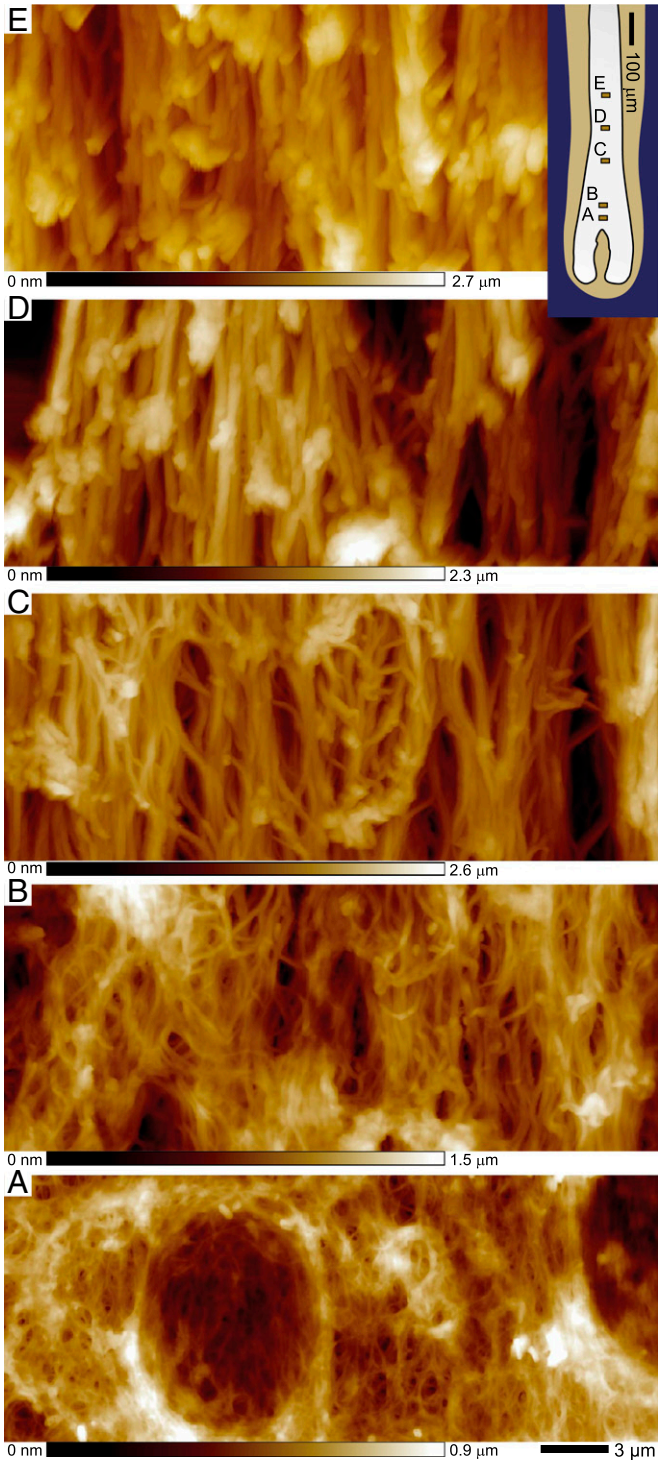

Fig. 2. Structural changes in the macrofibril network along the hair follicle. AFM topographic images taken along the follicle axis at increasing distances from the bulb. The *Inset* positions the recorded locations along the follicle axis, which are also shown in Fig. 1*A*. Note the evolution of macrofibril diameters and alignment.

Effect of Cysteine Cross-Linking and (Supra)Molecular Structure on Network Mechanics. The mechanics of a bionetwork are not only determined by its geometrical factors and the fiber concentration but also by the stiffness of the individual fibers. The microscopic network alterations of the fiber diameter and orientation slow down after the inflection point k of the stiffness curve around 500 µm above the bulb (Fig. 3). To better understand the still considerable increase of the elastic modulus that occurs after the inflection point, we studied the molecular substructure of the macrofibrils using X-ray microdiffraction. The small-angle and wide-angle X-ray diffraction (SAXS/WAXS) mappings of two follicles were analyzed as previously described (21), and the approximate positions of the four distinct keratinization zones (explained in Fig. S7) are reported in Fig. 4*B*. A comparison with the mechanical mapping on follicles of the same donor (Fig. 4*C*) shows that a fivefold stiffening occurs in zone I that contains nonoriented, amorphous structures. Zone II and zone III, which show IF formation, orientation, and later condensation into a network, each correspond to a 10-fold increase in modulus. Little stiffening occurs in zone IV that corresponds to the final axial rearrangement of the IFs within the macrofibrils. The keratin fibers in differentiated wool and hair contain a high amount of cysteine residues. Together with cysteine-rich KAPs, this ensures a covalent cross-linking of the IFs (31). Evidence of a gradual constitution of this disulfide keratin-KAP network was shown by X-ray diffraction in the late hair follicle (21). These observations indicate that cysteine formation and final axial rearrangement together with drying of the structure leads to the final stiffening.

To test the influence of cysteine cross-linking on the network stability, the mechanics of the follicle was probed before and after reduction by DTT. DTT is a reducing agent breaking cysteine-disufide bonds and causes macrofibril swelling evidenced by topographic AFM images (Fig. 5 *A* and *B*). Fig. 5*C* shows the mechanical mapping of a representative follicle before (black) and 3 h after addition of DTT (red). The measured modulus in the bulb is not affected by the addition of DTT (Fig. 5*D*; $n = 9$; 30 ± 23 vs. 24 ± 15 kPa). In contrast, DTT softens the network in the differentiated hair (Fig. 5*E*, gray lines). Note that the inflection point k (570 ± 214 µm) and the parameter n (3.1 ± 0.7)

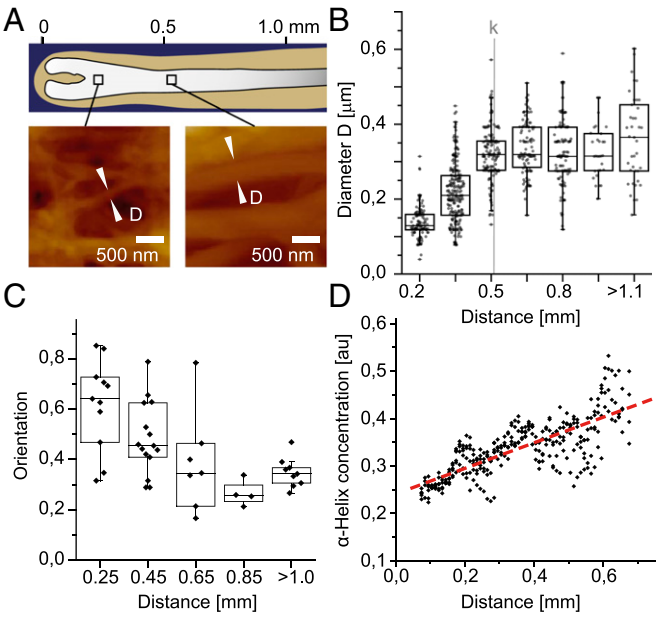

Fig. 3. Quantification of changes in the network architecture. (*A*) Quantification of macrofibril diameters D on randomly chosen and zoomed positions along the follicle using the AFM height profiles. (*B*) Boxplots of macrofibril diameters in dependency on their distance along the follicle axis. The average inflection point k for the mechanical stiffening is shown as gray line. (*C*) Preferential network orientation given by the ratio of the shortest to the longest decay of the autocorrelation function calculated for different angles. Values close to 1 indicate an isotropic picture, whereas values close to 0 indicate a preferred direction. (*D*) α-Helical protein concentration (1,652-cm^{-1} band) measured by synchrotron FT-IR microspectroscopy along the follicle.

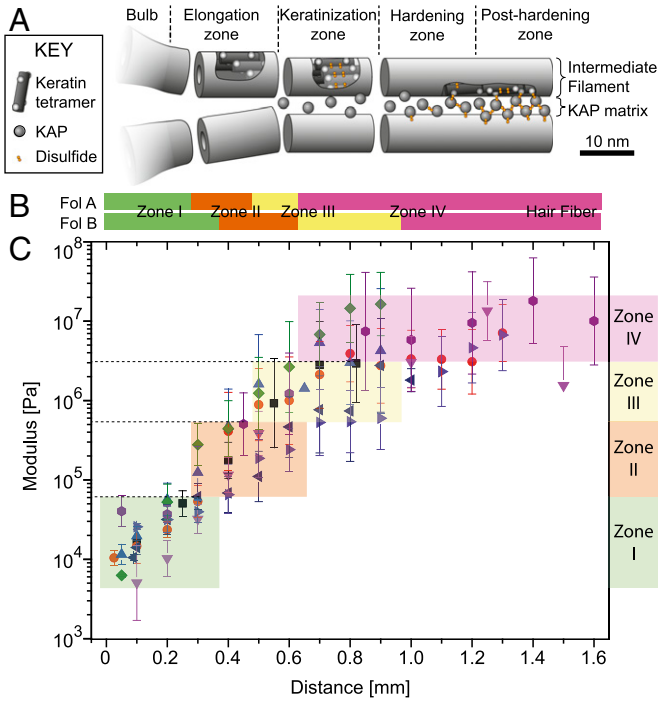

Fig. 4. Correlation between the mechanical characterization of the hair follicle and structural information given by XRD mapping. (*A*) Cartoon of the supramolecular organization of IFs and KAPs within the four zones defined by XRD studies (adapted from ref. 21). (*B*) Positions of the four zones on two dried follicles (*A* and *B*), both from the same donor determined with XRD. The experimental identification of the four zones is detailed in *SI Text* and Fig. S7. (*C*) Modulus maps for eight hydrated sections of five different follicles of the same donor used for the XRD study. Each point is the mean ± SD of 256 single force-indentation curves measured in a 10 × 10-μm^2 zone.

obtained by fitting the Hill function to the AFM data (*SI Text*) of DTT-treated follicles show no significant difference compared with the untreated ones (511 ± 150 μm and 3.7 ± 1.0, respectively). A plot of the moduli ratios of individual control to DTT-treated follicles (Fig. 5*F*) revealed that cysteine cross-linking exerts a continuously increasing influence on the elastic moduli along the follicle axis. The first notable effects of DTT occur at around 400–500 μm, followed by a gradual increase, up to three- to fourfold due to cysteine cross-linking in the differentiated hair.

Discussion

Our results represent, to our knowledge, the first measurement of the gradual stiffening of the hair fiber over the course of the entire keratinization process within the hair follicle. We will now put the mechanical measurements into perspective with concomitant changes in the microscopic network architecture, supramolecular organization of the local keratin, and biological events (Fig. 4).

Our AFM and TEM data show that an isotropic IF network appears right above the dermal papilla, within the elongation zone (zone I; Fig. 4) ~200 μm from the base of the follicle (Fig. 2*A* and Fig. S2) (30). The observed appearance of the IF network is consistent with previous reports on the formation of keratins such as K35 and K85 (32, 33), together with high-glycine-tyrosine and high-sulfur KAPs in the early zone I, just above the dermal papilla (19). Our DTT reduction experiments revealed that cysteine cross-linking does not significantly contribute to mechanical properties at this stage (Fig. 5*D*). We hypothesize that this early network is rather stabilized by isopeptide (γ-glutamyl-ε-lysine) bonds between early KAPs and keratins, enabled by the previously established expression and activity of transglutaminase 3 at the base of the hair follicle (34).

From zone I on until the end of zone III (~800 μm from the bulb), we observe a continuous mechanical stiffening of the network following a power law (Fig. 1*D*). During zones I and II, the IFs start forming a network of small macrofibrils that grow in diameter by lateral aggregation (Fig. 2 and 3*B*) (21, 35, 36). Also a gradual increase in volume fraction occupied by the macrofibrils occurs (Fig. S3*B*), along with a progressive orientation of the microscopic network as observed by AFM (Fig. 3*C*) and an increasing polarization of supercoiled keratin coils as determined by X-ray diffraction (XRD; Fig. 4). Together, these observations indicate that a significant portion of the proteins required to form the mature hair are assembled into macrofibrils by the end of zone II and mostly held by a transglutaminase-based network, which is consistent with the absence of further changes in the type of expressed keratins from zone III onward (37). We can theoretically model the related mechanical stiffening within the regions I and II by using an isotropic semiflexible, cross-linked 3D network model (4, 38) (*SI Text*) where nonaffine fiber bending is the dominant elastic mechanism. In such nonthermal networks, the network mesh size has to be smaller than the fiber persistence length, which we deduce from the macrofibril architecture within zones I and II (*SI Text*). These nonthermal models are common to fibrous tissues

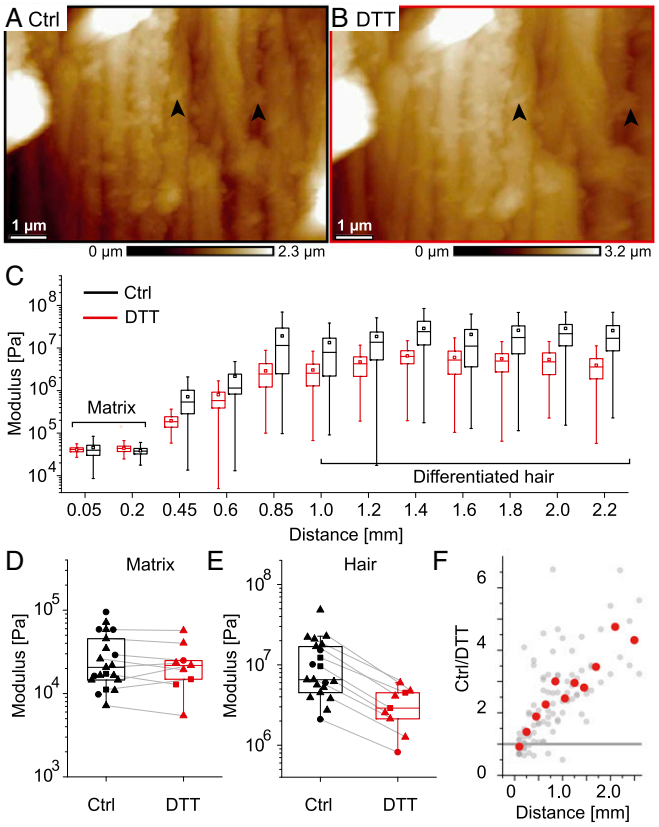

Fig. 5. Effect of cysteine cross-linking on macrofibril morphology and follicle mechanics. AFM topographic images of the same region of a follicle section in PBS (*A*) and after cystine reduction by DTT (*B*). Arrows highlight the same distinct features before and after DTT treatment. (*C*) Representative mechanical mapping along one follicle before (black) and 3 h after addition of 300 mM DTT (red). (*D*) Boxplots of mean stiffness modulus determined in the matrix of different follicles before and after DTT reduction. The gray lines connect points obtained from the same follicle (n = 9). (*E*) Boxplots of mean values measured in the differentiated hair (distances > 800 μm) of different follicles before and after addition of DTT (n = 9). (*F*) Ratio of untreated to treated mean moduli for each individual follicle according to the distance from the bulb along the follicle axis (gray points). Red points show averages within bins of 200 μm.

such as collagen (39) and differ from other models used, e.g., to describe actin networks (11, 12). In a bending dominated network, the Young's modulus scales with $E \approx 3G \sim \kappa/l_0^4 \sim E_f(r^4/l_0^4)$, where E_f denotes the modulus, r denotes the radius of a single macrofiber, and l_0 denotes the distance between vertices (4, 38). The linearly increasing radius of the macrofibers along the follicle axis during zones I and II (Fig. 3*B*) ($r = \text{const}\, x$), alone would therefore be sufficient to explain the network's increase in elastic modulus following a powerlaw with an exponent of 4, which is close to our observed value of 4.4.

However, the macrofibrils reach their maximum diameter in late zone II (~500 μm; Fig. 3*B*), whereas the mechanical stiffening is still ongoing. This continued stiffening can thus not be explained by the above model and suggests additional contributions to the hardening, such as an increasing network orientation and compaction and internal mechanical reinforcement of the macrofibrils by disulfide cross-links. The internal reinforcement of the macrofibrils might be driven by a continued synthesis of KAPs (especially of the ultra-high-sulfur family) until late zone III as shown by in situ hybridization studies (19), suggesting a continued influx of KAPs into the macrofibrils. In agreement, XRD experiments revealed a gradual appearance of the KAP/IF quasi-hexagonal network and final maturation of the IF internal structure in zone III, after 500–700 μm. Our DTT reduction experiments show that a significant contribution of disulfide bonds to the overall network mechanics becomes visible already in zone II (Fig. 5*F*), whereas the matrix architecture there is far from being complete because most of the KAP/IF disulfide bonds are constituted much further up the follicle (in zone IV, 650 μm at earliest) (21). Those early disulfides should therefore mainly represent intra-IF disulfides (40), which contribute to the overall mechanical properties of the macrofibril. It is plausible that this intra-IF disulfide formation constitutes the driving force that leads to the maturation of the IFs in this area of the follicle (21, 41). This picture is in agreement with recent work by Fraser and Parry (42), establishing that the maturation of the IFs in zone III should be accompanied by an alignment of intra-IF cysteine moieties to enable such crosslinks.

Within zone IV (from 800 μm on), we found that the modulus of the hair fiber only slightly increased (by a factor of 2). For a follicle immersed in PBS, the mechanical maturation is therefore finished from 1,000 μm on above the bulb. The measured plateau of the mechanical modulus is consistent with the observation that the modulus of ~11 MPa that we observed at the end of zone IV is very close to the estimated value of ~6–9 MPa for a single IF in aqueous solution (10, 43, 44). This, together with closely packed fiber organization, suggests a transition to a stretching–dominated network, in opposition to zones I and II where the network mechanics were bending dominated. However, the effect of DTT on the follicle mechanics at 1,500 μm is twice as much as that at 800 μm (Fig. 5*D*), indicating further changes in the network. X-ray microdiffraction results show that the formation of the KAP/IF disulfide network evidenced by the strengthening of the 67-Å reflection is the only structural rearrangement occurring above 800 μm (Fig. 4) (20, 21). This low influence of the IF/KAP disulfide network on the follicle mechanics, despite its extremely high density, is likely a consequence of the immersion in PBS during our experiments. Due to the hygroscopic nature of the KAP matrix, it will swell in water, whereas the IFs show only little water uptake (45), causing a weakening of ionic and H-bond interactions. This swelling could minimize the mechanical contribution of the matrix in our measurements. To confirm this, AFM measurements were performed on the same follicles after drying, leading to values of moduli of 2.7 ± 1.4 GPa (Fig. 1*B*) at positions >800 μm. These values are comparable to those measured on mature dry hair using microindentation techniques and AFM (16, 28). This high Young's modulus indicates that the final rearrangement of the KAP/IF disulfide network together with the loss of water finalizes the keratinization process of the hair fiber.

Conclusion

Our observations link changes in the architecture and molecular structure of keratin macrofibrils to the local mechanical behavior at a tissue scale level. The complex simultaneous changes including macrofibril thickening, fiber orientation, and keratinization leads to an increase in stiffness by three orders of magnitude in just over the course of 1 mm. Our results are fully consistent with the existing structural and biological literature on the hair follicle and are also compatible with theoretical models relating structure and mechanical properties. Moreover, we further substantiate the hypothesis of an isopeptide network scaffold to stabilize the early keratin macrofibrils and propose a sequence of disulfide network formation events thereafter.

Materials and Methods

Sample Preparation. Individual human terminal anagen hair follicles were obtained from facelift surgery, dissected, and stored at –80° in TissueTek (Sakura Finetek). Longitudinal 10-μm-thick sections were obtained using a Leica CM3050 Cryotome at –30°. For AFM studies, the slices were adsorbed on glass coverslips and immediately placed in PBS (Gibco). For FTIR microspectroscopy studies, sections were deposited on BaF_2 slides and dried. For XRD mapping, the follicles were inserted in a glass capillary and dried before analysis.

Mechanical Mapping of Follicles Using AFM. Mechanical quantification of the hair follicle with force volume mode was either done in PBS on the DimensionIcon AFM (Bruker) using a ScanAsyst-Fluid lever ($k_c \sim 1$ N/m, r = 20–60 nm) at room temperature or in dried conditions using the stiffer RTESPA (k_c ~40 N/m, r = 8 nm) or TAP525A (k_c ~200 N/m, r = 8 nm) levers (Bruker). In the force volume mode, 256 equidistant force-indentation traces with constant velocity are recorded with 5,000 points per trace within a 10 × 10-μm^2 zone. Traces are fitted with the Hertz model to obtain the mean Young's modulus within one zone. The lever calibration and the details for the determination of macroscopic moduli within a 10 × 10-μm^2 zone are detailed in *SI Text*.

Topographic Imaging Using AFM. Topographic imaging was performed with the Peak Force QNM mode with a scanning frequency of 0.1 Hz/line and a peak force of ~6 nN on the DimensionIcon AFM. When measuring in PBS solution the ScanAsyst-Fluid+ lever (k_c = 0.7 N/m, r = 2 nm) was used, and the ScanAsyst-Air lever (k_c = 0.4 N/m, r = 2 nm) was used when measuring in dry conditions.

Infrared Spectroscopy. Follicles were characterized at the SOLEIL Synchrotron on the SMIS beamline. The setup consists of a Nicolet 5700 FTIR spectrometer (Thermo Fisher) equipped with a Michelson interferometer and a KBr beam splitter, a Prior XYZ motorized stage, and a Continuum XL microscope (Thermo Fisher) used in confocal/transmission mode. The aperture was set at 10 × 10 μm^2. Spectra were recorded at 4-cm^{-1} resolution and treated using Omnic (Thermo Fisher) and The Unscrambler (Camo) software. Collections of nonsaturated spectra were baseline corrected to remove artifacts within the amide 1 region (1,720–1580 cm^{-1}), and thickness corrected to offset variations in sample thickness using measurements performed with an NT9100 optical profilometer (Bruker).

X-Ray Microdiffraction Studies. The follicles were characterized at the European Synchrotron Radiation Facility (ESRF) Synchrotron on the ID13 beamline (beam wavelength, 0.8556 Å; dimensions, 1.6 × 3 μm^2). The experiments were carried out with a 117.5-mm sample–detector distance, which was calibrated using silver behenate (first order of 58.38 Å). Patterns were recorded on a CCD FRELON detector (2,048 × 2,048 pixels; pixel size of 50 × 50 μm^2). Exposure time was set at 1 s, which caused no radiation damage.

About 1,800 diffractograms were collected on each follicle, by conducting a mapping with a lateral step of 5 μm and a longitudinal step of 50 μm in the first 1.5 mm from the base of the follicle and 250-μm step thereafter. The four keratinization zones were located according to the criteria described in ref. 21 that are recalled in *SI Text* and Fig. S7.

ACKNOWLEDGMENTS. Ramona Enea-Casse is acknowledged for granting access to the AFM. Christophe Sandt (SMIS beamline, Synchrotron SOLEIL) is thanked for assistance during the experiments and data analysis and discussion. Bernard Querleux is acknowledged for critical reading of the manuscript. We thank Frédéric Leroy for support in setting up this project.

1. Levental I, Georges PC, Janmey PA (2007) Soft biological materials and their impact on cell function. *Soft Matter* 3(3):299–306.
2. Bar-On B, Wagner HD (2013) Structural motifs and elastic properties of hierarchical biological tissues - a review. *J Struct Biol* 183(2):149–164.
3. Meyers MA, McKittrick J, Chen PY (2013) Structural biological materials: Critical mechanics-materials connections. *Science* 339(6121):773–779.
4. Pritchard RH, Huang YY, Terentjev EM (2014) Mechanics of biological networks: From the cell cytoskeleton to connective tissue. *Soft Matter* 10(12):1864–1884.
5. Picu RC (2011) Mechanics of random fiber networks-a review. *Soft Matter* 7(15): 6768–6785.
6. Huber F, et al. (2013) Emergent complexity of the cytoskeleton: From single filaments to tissue. *Adv Phys* 62(1):1–112.
7. Janmey PA, Winer JP, Murray ME, Wen Q (2009) The hard life of soft cells. *Cell Motil Cytoskeleton* 66(8):597–605.
8. Köster S, Weitz DA, Goldman RD, Aebi U, Herrmann H (2015) Intermediate filament mechanics in vitro and in the cell: From coiled coils to filaments, fibers and networks. *Curr Opin Cell Biol* 32(0):82–91.
9. Piechocka IK, Bacabac RG, Potters M, Mackintosh FC, Koenderink GH (2010) Structural hierarchy governs fibrin gel mechanics. *Biophys J* 98(10):2281–2289.
10. Fudge DS, et al. (2009) From ultra-soft slime to hard alpha-keratins: The many lives of intermediate filaments. *Integr Comp Biol* 49(1):32–39.
11. Gardel ML, et al. (2004) Elastic behavior of cross-linked and bundled actin networks. *Science* 304(5675):1301–1305.
12. Lieleg O, Claessens MMAE, Heussinger C, Frey E, Bausch AR (2007) Mechanics of bundled semiflexible polymer networks. *Phys Rev Lett* 99(8):088102.
13. Yang W, et al. (2015) On the tear resistance of skin. *Nat Commun* 6:6649.
14. Shin JH, Gardel ML, Mahadevan L, Matsudaira P, Weitz DA (2004) Relating microstructure to rheology of a bundled and cross-linked F-actin network in vitro. *Proc Natl Acad Sci USA* 101(26):9636–9641.
15. Sander EA, Stein AM, Swickrath MJ, Barocas VH (2010) Out of many, one: Modeling schemes for biopolymer and biofibril networks. *Trends in Computational Nanomechanics, Challenges and Advances in Computational Chemistry and Physics*, ed Dumitrica T (Springer, Dordrecht, The Netherlands), 9th Ed, pp 557–602.
16. Wei G, Bhushan B, Torgerson PM (2005) Nanomechanical characterization of human hair using nanoindentation and SEM. *Ultramicroscopy* 105(1-4):248–266.
17. Luengo GS, Galliano A (2013) *Applications of Scanning Probe Methods in Cosmetic Science. Scanning Probe Microscopy in Industrial Applications* (John Wiley & Sons, New York), pp 270–286.
18. Birbeck MS, Mercer EH (1957) The electron microscopy of the human hair follicle. I. Introduction and the hair cortex. *J Biophys Biochem Cytol* 3(2):203–214.
19. Rogers MA, Langbein L, Praetzel-Wunder S, Winter H, Schweizer J (2006) Human hair keratin-associated proteins (KAPs). *International Review of Cytology*, ed Jeon KW (Academic Press, New York), Vol 251, pp 209–263.
20. Baltenneck F, et al. (2000) Study of the keratinization process in human hair follicle by X-ray microdiffraction. *Cell Mol Biol (Noisy-le-grand)* 46(5):1017–1024.
21. Rafik ME, Briki F, Burghammer M, Doucet J (2006) In vivo formation steps of the hard alpha-keratin intermediate filament along a hair follicle: Evidence for structural polymorphism. *J Struct Biol* 154(1):79–88.
22. Morioka K (2009) A guide to hair follicle analysis by transmission electron microscopy: Technique and practice. *Exp Dermatol* 18(7):577–582.
23. Cohen SR, Kalfon-Cohen E (2013) Dynamic nanoindentation by instrumented nanoindentation and force microscopy: A comparative review. *Beilstein J Nanotechnol* 4:815–833.
24. Hertz H (1881) Über die Berührung fester elastischer Körper. *J Reine Angew Math* 92: 156–171.
25. Loparic M, et al. (2010) Micro- and nanomechanical analysis of articular cartilage by indentation-type atomic force microscopy: Validation with a gel-microfiber composite. *Biophys J* 98(11):2731–2740.
26. Stolz M, et al. (2004) Dynamic elastic modulus of porcine articular cartilage determined at two different levels of tissue organization by indentation-type atomic force microscopy. *Biophys J* 86(5):3269–3283.
27. Vargas-Pinto R, Gong H, Vahabikashi A, Johnson M (2013) The effect of the endothelial cell cortex on atomic force microscopy measurements. *Biophys J* 105(2): 300–309.
28. Fortier P, Suei S, Kreplak L (2012) Nanoscale strain-hardening of keratin fibres. *PLoS One* 7(7):e41814.
29. Swift JA (1977) The histology of keratin fibers. *Chemistry of Natural Protein Fibers*, ed Asquith RS (Springer, New York), pp 81–146.
30. Marshall RC, Orwin DFG, Gillespie JM (1991) Structure and biochemistry of mammalian hard keratin. *Electron Microsc Rev* 4(1):47–83.
31. Deb-Choudhury S, et al. (2015) Mapping the accessibility of the disulfide crosslink network in the wool fiber cortex. *Proteins* 83(2):224–234.
32. Langbein L, et al. (1999) The catalog of human hair keratins. I. Expression of the nine type I members in the hair follicle. *J Biol Chem* 274(28):19874–19884.
33. Langbein L, Rogers MA, Winter H, Praetzel S, Schweizer J (2001) The catalog of human hair keratins. II. Expression of the six type II members in the hair follicle and the combined catalog of human type I and II keratins. *J Biol Chem* 276(37):35123–35132.
34. Thibaut S, et al. (2009) Transglutaminase-3 enzyme: A putative actor in human hair shaft scaffolding? *J Invest Dermatol* 129(2):449–459.
35. Parry DAD, Strelkov SV, Burkhard P, Aebi U, Herrmann H (2007) Towards a molecular description of intermediate filament structure and assembly. *Exp Cell Res* 313(10): 2204–2216.
36. John McKinnon A, Harland DP (2011) A concerted polymerization-mesophase separation model for formation of trichocyte intermediate filaments and macrofibril templates. 1: Relating phase separation to structural development. *J Struct Biol* 173(2):229–240.
37. Thibaut S, et al. (2003) Hair keratin pattern in human hair follicles grown in vitro. *Exp Dermatol* 12(2):160–164.
38. Broedersz CP, Sheinman M, Mackintosh FC (2012) Filament-length-controlled elasticity in 3D fiber networks. *Phys Rev Lett* 108(7):078102.
39. Arevalo RC, Urbach JS, Blair DL (2010) Size-dependent rheology of type-I collagen networks. *Biophys J* 99(8):L65–L67.
40. Popescu C, Höcker H (2009) Cytomechanics of hair: Basics of the mechanical stability. *International Review of Cell and Molecular Biology International Review of Cell and Molecular Biology*, ed Jeon KW (Academic Press, New York), Vol 277, pp 137–156.
41. Fraser RDB, Parry DAD (2007) Structural changes in the trichocyte intermediate filaments accompanying the transition from the reduced to the oxidized form. *J Struct Biol* 159(1):36–45.
42. Bruce Fraser RD, Parry DAD (2012) The role of disulfide bond formation in the structural transition observed in the intermediate filaments of developing hair. *J Struct Biol* 180(1):117–124.
43. Lin YC, et al. (2010) Origins of elasticity in intermediate filament networks. *Phys Rev Lett* 104(5):058101.
44. Fudge DS, Gardner KH, Forsyth VT, Riekel C, Gosline JM (2003) The mechanical properties of hydrated intermediate filaments: Insights from hagfish slime threads. *Biophys J* 85(3):2015–2027.
45. Kreplak L, et al. (2002) A new deformation model of hard alpha-keratin fibers at the nanometer scale: Implications for hard alpha-keratin intermediate filament mechanical properties. *Biophys J* 82(4):2265–2274.
46. MacKintosh FC, Käs J, Janmey PA (1995) Elasticity of semiflexible biopolymer networks. *Phys Rev Lett* 75(24):4425–4428.
47. Pawelzyk P, Mücke N, Herrmann H, Willenbacher N (2014) Attractive interactions among intermediate filaments determine network mechanics in vitro. *PLoS One* 9(4): e93194.
48. Yamada S, Wirtz D, Coulombe PA (2003) The mechanical properties of simple epithelial keratins 8 and 18: Discriminating between interfacial and bulk elasticities. *J Struct Biol* 143(1):45–55.
49. Hutter J, Bechhoefer J (1993) Calibration of atomic force microscope tips. *Rev Sci Instrum* 64(7):1868–1873.
50. Burnham NA, et al. (2003) Comparison of calibration methods for atomic-force microscopy cantilevers. *Nanotechnology* 14(1):1–6.
51. Love AEH (1939) Boussinesq's problem for a rigid cone. *Q J Math* 10(1):161–175.
52. Sneddon IN (1965) The relation between load and penetration in the axisymmetric boussinesq problem for a punch of arbitrary profile. *Int J Eng Sci* 3(1):47–57.
53. Costa KD, Yin FCP (1999) Analysis of indentation: Implications for measuring mechanical properties with atomic force microscopy. *J Biomech Eng* 121(5):462–471.
54. Ohashi T, Ishii Y, Ishikawa Y, Matsumoto T, Sato M (2002) Experimental and numerical analyses of local mechanical properties measured by atomic force microscopy for sheared endothelial cells. *Biomed Mater Eng* 12(3):319–327.
55. Guz N, Dokukin M, Kalaparthi V, Sokolov I (2014) If cell mechanics can be described by elastic modulus: Study of different models and probes used in indentation experiments. *Biophys J* 107(3):564–575.
56. Radmacher M, Fritz M, Hansma PK (1995) Imaging soft samples with the atomic force microscope: Gelatin in water and propanol. *Biophys J* 69(1):264–270.
57. Johnson KL, Kendall K, Roberts AD (1971) Surface energy and the contact of elastic solids. *Proc R Soc Lond A: Math Physic Eng Sci* 324(1558):301–313.
58. Derjaguin BV, Muller VM, Toporov Y (1975) Effect of contact deformations on the adhesion of particles. *J Colloid Interface Sci* 53(2):314–326.
59. Bilodeau GG (1992) Regular pyramid punch problem. *J Appl Mech* 59(3):519–523.